Journal of Magnetic Resonance **137,** 186–195 (1999)
Article ID jmre.1998.1665, available online at http://www.idealibrary.com on IDEAL®

Pulsed Field Gradients in Simulations of One- and Two-Dimensional NMR Spectra

Ghirmai H. Meresi, Miroslava Cuperlovic, William E. Palke,[1] and J. T. Gerig[1]

Department of Chemistry, University of California, Santa Barbara, Santa Barbara, California 93106

Received July 23, 1998; revised November 6, 1998

A method for the inclusion of the effects of *z*-axis pulsed field gradients in computer simulations of an arbitrary pulsed NMR experiment with spin $\frac{1}{2}$ nuclei is described. Recognizing that the phase acquired by a coherence following the application of a *z*-axis pulsed field gradient bears a fixed relation to its order and the spatial position of the spins in the sample tube, the sample is regarded as a collection of volume elements, each phase-encoded by a characteristic, spatially dependent precession frequency. The evolution of the sample's density matrix is thus obtained by computing the evolution of the density matrix for each volume element. Following the last gradient pulse, these density matrices are combined to form a composite density matrix which evolves through the rest of the experiment to yield the observable signal. This approach is implemented in a program which includes capabilities for rigorous inclusion of spin relaxation by dipole–dipole, chemical shift anisotropy, and random field mechanisms, plus the effects of arbitrary RF fields. Mathematical procedures for accelerating these calculations are described. The approach is illustrated by simulations of representative one- and two-dimensional NMR experiments. © 1999 Academic Press

Key Words: **coherence selection; dipole–dipole relaxation; (DQFC) double quantum-filtered COSY; (HSQC) heteronuclear single quantum coherence; NOE; propagators; pulsed field gradients; relaxation; relaxation cross terms; spectral simulation; spin echo.**

INTRODUCTION

The use of pulsed field gradients in NMR experiments dates back over decades to the work of Stejskal and Tanner (*1*) with their seminal paper for the measurement of diffusion constants. Many years later, Maudsley *et al.* (*2*) and Bax *et al.* (*3, 4*) demonstrated the use of gradients for coherence pathway selection. Solution of a number of technical problems, primarily the nonreproducibility of gradient pulses and the effect of perturbing magnetic fields generated in nearby conductors by eddy currents (*5, 6*), led to the pioneering work by Hurd *et al.* (*7, 8*) and by van Zijl and Moonen (*9, 10*) that established the efficacy of pulsed field gradients in high-resolution NMR experiments. Gradient experiments are now often the methods of choice for coherence pathway selection (*11, 12*), solvent signal suppression (*13, 14*), selective excitation (*15*), phase cycle elimination or reduction, and artifact elimination (*16, 17*). Basic considerations in the use of pulsed field gradients have been reviewed (*12, 18*), as has the application of gradients in multidimensional studies of biological systems (*19*).

Hardware developments have now reached a stage where artifact-free multidimensional high-resolution NMR experiments that use pulsed field gradients are routine. In contrast, available computer techniques for simulation of the results of such experiments have not kept pace. Dozens of NMR simulation programs are, of course, available from instrument manufacturers, from the World Wide Web, or by private arrangements. Most of these include relaxation in a nonrigorous way (typically via an effective T_1 or T_2 relaxation time) or do not provide capabilities to take into account other experimental considerations such as finite RF power. We are unaware of any computer simulation capabilities for experiments that include pulsed field gradients and treat relaxation in a rigorous manner.

The present work enables computer simulations of arbitrary experiments that include nuclear spin relaxation effects (dipole–dipole, chemical shift anisotropy, and random field mechanisms, as well as cross terms between dipole–dipole and CSA mechanisms), cw and pulsed RF fields, and *z*-axis pulsed field gradients. In describing the approach taken, we first establish our notation and obtain analytical results for the effects of the pulsed field gradients on the density matrix. Next the validity of our method and its dependence on various simulation parameters are explored. In the last section, we illustrate the application of the code developed to simulations of several one- and two-dimensional spectra. It is concluded that the rather straightforward approach we describe rapidly provides reliable simulations of high-resolution NMR experiments that employ *z*-axis pulsed field gradients.

THEORETICAL BACKGROUND

Any NMR experiment is a sequence of time intervals during which the spins may experience the application of various static or time-varying fields or may simply be undergoing spontaneous processes such as Larmor precession or relaxation. In a simulation of an experiment, the behavior of the spins during each of these periods is calculated in series, by

[1] To whom correspondence should be addressed. Fax: 805/893-4120; E-mail: palke@nmr.ucsb.edu and gerig@nmr.ucsb.edu.

1090-7807/99 $30.00

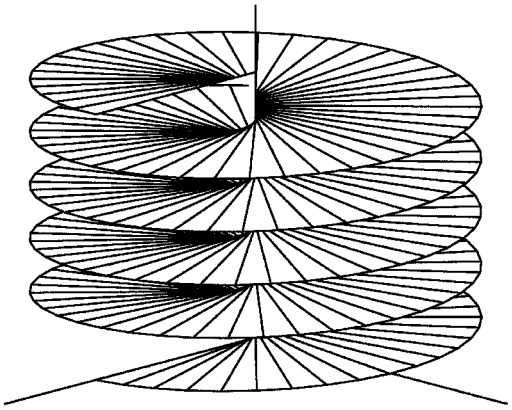

FIG. 1. A representation of the orientations of a collection of magnetization vectors following the application of a 90° pulse and a pulsed field gradient. The pitch of the helix is determined by the gradient pulse length, the gradient strength, and the gyromagnetic ratio of the spins.

following the evolution of the density matrix. A field gradient pulse is an interval during which the static external magnetic field is rendered deliberately spatially inhomogeneous. We will consider only linear gradients along the z-axis. Hence, the gradient field can be written as Gz, with G being the (constant) gradient strength in tesla/meter, and the z-coordinate is measured in meters. The effect of the gradient can be visualized by recognizing that at each value of z the sample experiences a characteristic magnetic field during the gradient pulse. The precession rate of a coherence will depend on the z-coordinate so that after a gradient pulse of duration τ, the phase of a p-quantum coherence will be arranged in a helical pattern whose pitch is determined by $\gamma G\tau p$, with γ being the gyromagnetic ratio of the nucleus (*18, 20*). This effect of a linear z-axis gradient is illustrated in Fig. 1.

For a simulation, we divide the region of interest into N segments and follow the density matrix $\sigma(k)$ for the kth segment ($0 \leq k \leq [N-1]$) through the experiment. No spatial inhomogeneity is generated in the sample until the first gradient pulse, and up to that point in the simulation the density matrices of all volume elements will be identical and essentially equal to the density matrix representing the entire sample. Calculation of evolutions in response to pulses, delays, or other gradient pulses after the first gradient pulse proceeds for each slice separately. At the end of the final gradient, the density matrices from the N segments are combined to yield the complete system density matrix. Calculation of the evolution of the complete density matrix generates the expected detectable signal. Performing the summation over segments prior to the final gradient results in loss of memory of the phase encoding that is indicated in Fig. 1.

The full Hamiltonian for a nuclear spin system in the presence of a static external magnetic field, magnetic field gradients, and a radiofrequency field can be written as (*20–24*)

$$H(t) = H_0 + H_G + H_1(t) + H_2(t). \qquad [1]$$

The first time-independent term consists of the Zeeman, scalar coupling, and isotropic chemical shielding terms:

$$H_0 = -\hbar B_0 \sum_i^{\text{spins}} \gamma_i[1 - \sigma_{\text{iso}}(i)]I_Z(i) + \sum_i^{\text{spins}} \sum_{j>i}^{\text{spins}} J_{\text{iso}}(ij)\mathbf{I}(\text{i}) \cdot \mathbf{I}(j). \qquad [2]$$

The second term in Eq. [1] describes the interaction of the spins with the external magnetic field gradient; it is different for each slice, and for the kth slice it is given by

$$H_G(k) = -\hbar Gz(k) \sum_i^{\text{spins}} \gamma_i[1 - \sigma_{\text{iso}}(i)]I_Z(i), \qquad [3]$$

where G is the strength of the magnetic field gradient and $z(k)$ denotes the z-coordinate of the kth slice in the sample tube. It is worth noting that the gradient Hamiltonian has the same form as the Zeeman term except for its dependence on coordinate z. The third term in Eq. [1] describes the interaction of the spins with the radiofrequency pulses,

$$H_1(t) = -\hbar B_{\text{rf}} e^{iF_Z\Omega_{\text{rf}}t/\hbar} M_\phi e^{-iF_Z\Omega_{\text{rf}}t/\hbar}, \qquad [4]$$

where B_{rf} is the amplitude of the RF field, and Ω_{rf} is its angular frequency. M_ϕ is the component of the magnetic moment along ϕ in the xy-plane and is related to the spin angular momentum operators by

$$M_\phi = R_Z(\phi) \sum_i^{\text{spins}} \gamma_i I_X(i) R_Z^{-1}(\phi), \qquad [5]$$

where $R_Z(\phi) = e^{-i\phi F_Z/\hbar}$. The remaining term in Eq. [1] is also time-dependent and arises from interactions that can produce spin relaxation.

The time evolution of the nuclear spin density matrix is governed by the Liouville–von Neumann equation (*20–24*):

$$i\hbar \frac{\partial \sigma}{\partial \text{t}} = [H, \sigma]. \qquad [6]$$

Including the effects of relaxation in the solution of this equation is computationally costly, typically requiring the diagonalization of a Redfield (*25*) matrix of dimensions $2^{2n} \times 2^{2n}$, with n being the number of nuclei in the spin system. Especially because our treatment of gradients requires the solution of Eq. [6] separately for each slice along the z-axis in the sample, an efficient procedure must be devised for this

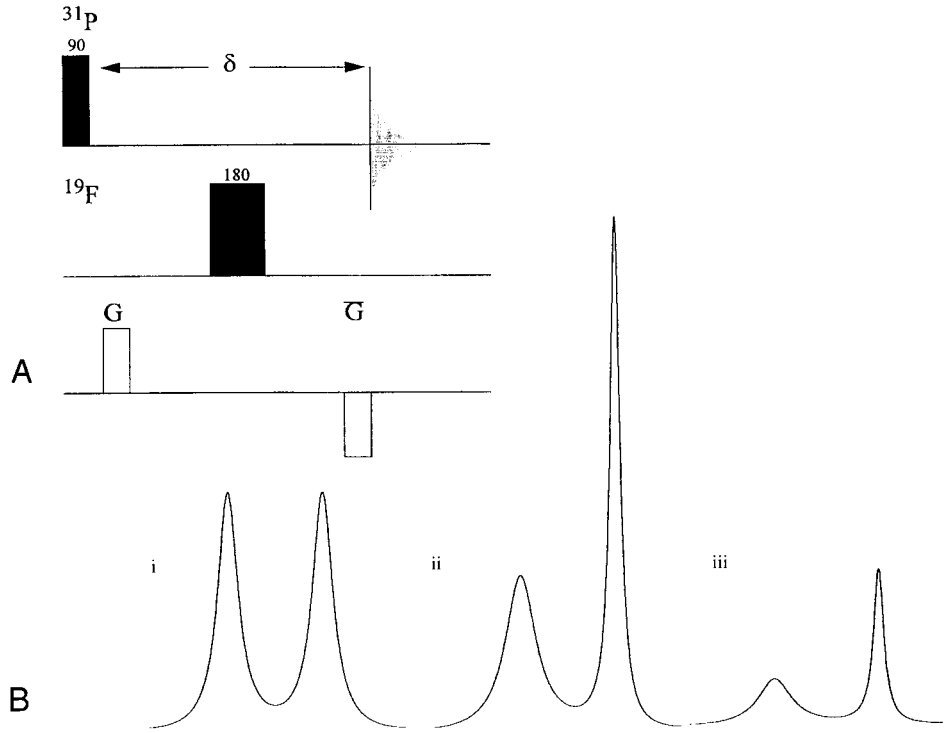

FIG. 2. (A) Pulse sequence used for simulation of a phosphorus gradient-recalled echo experiment with the protein-bound fluorophosphate (P-F) system described by Withers *et al.* (*29*). The phosphorus frequency was 109 MHz, CSA parameters for fluorine and phosphorus were taken from the compilation by Duncan (*30*), and $J_{PF} = -890$ Hz. A rotational correlation time (τ_c) of 73 ns and gradients of ± 2 G/cm with 20 slices were used for the simulations. (B) Lineshapes obtained by Fourier transformation of the FID calculated for this system: (i) Fluorine and phosphorus CSA and dipolar contributions to relaxation are included, but cross terms between dipole and CSA terms are neglected; $\delta = 0.2$ ms; (ii) all fluorine and phosphorus CSA and dipolar contributions to relaxation are computed, including dipole–CSA cross terms; $\delta = 0.2$ ms; (iii) the same as for simulation (ii), but $\delta = 2.0$ ms. The vertical scale is the same for all plots. The observed lineshape is in rough accord with experimental observations.

purpose. Use of superoperator propagators is crucial in making this problem tractable, because it simplifies computation of the evolution of the density matrix to a simple matrix multiplication for each slice (*26, 27*). The extension of propagator methods to include relaxation was presented by Smith *et al.* (*28*). We discuss the relaxation propagator and explain our procedure for its implementation in Appendix A.

Computation of an FID, done point-by-point, is another repetitive and time-consuming aspect of the simulation of NMR experiments that is fruitfully approached in terms of a propagator. Appendix B describes our application of propagators to this situation.

COMPUTATIONAL STUDIES

It is helpful to consider an example in order to show how propagator techniques have been applied in this work to simulations of experiments involving gradient pulses. Suppose the experiment begins with the system at equilibrium and consists of three steps (pulses and/or delays) before the initial gradient. The effect of each step in the sequence is simply the matrix multiplication of the propagator for that step $\mathcal{P}_j$ times the density matrix at the start of that step. Thus, our density matrix at the end of the three preliminary steps is

$$\sigma = \mathcal{P}_3\mathcal{P}_2\mathcal{P}_1\sigma_{eq}. \quad [7]$$

Because a gradient pulse has a different effect on each slice of the sample, the propagator for a gradient $\mathcal{G}(k)$ depends on the slice index k. Hence, the density matrix after the first gradient also depends upon k:

$$\sigma(k) = \mathcal{G}_1(k)\mathcal{P}_3\mathcal{P}_2\mathcal{P}_1\sigma_{eq}. \quad [8]$$

If our initial gradient is followed by three more steps and then a final gradient, the density matrix for the complete system at the end of this entire sequence is the combination of the density matrices in each segment:

$$\sigma = \sum_{k=0}^{N-1} [\mathcal{G}_2(k)\mathcal{P}_6\mathcal{P}_5\mathcal{P}_4\mathcal{G}_1(k)\mathcal{P}_3\mathcal{P}_2\mathcal{P}_1] \frac{\sigma_{eq}}{N}. \quad [9]$$

This combined density matrix can then be followed through the

rest of the experiment. Throughout the calculation, efficiencies can be introduced. The propagator for any step that is to be repeated can be stored and reused; this includes any combinations of repeated steps. For example, the product of $\mathcal{P}_6\mathcal{P}_5\mathcal{P}_4$ can be evaluated and included as a single matrix multiplication.

In a simulation the entire range of phases produced by the gradients must be sampled, because it is through the cancellations and reinforcements of these phases that the gradients experimentally have their effect. Thus, in implementing Eq. [9], the simulation must sample the range of phases from 0 to $2m\pi$. An integral number of loops m of the helix must be included in order to sample these phases uniformly. It is also evident from Fig. 1 that additional loops of a particular helix of phase angles, e.g., $2\pi \leq \phi \leq 4\pi$, are redundant with the first loop. Consequently, full phase sampling might be achieved with surprisingly few slices. However, the number of helix loops and the number of segments required to sample phases reliably depend on the details of the spin system under consideration.

For a homonuclear system, single quantum coherences (1QC) precess at the slowest rate, so as a 1QC precesses through 2π, a homonuclear coherence of order p (pQC) precesses through $2p\pi$. If we let L be the number of loops used to represent a 1QC, the phase angles sampled for a simulation using N segments are (for a pQC)

$$\theta_k = \frac{2\pi pL}{N}k, \quad k = 0, 1, 2, \ldots, N-1. \qquad [10]$$

If the quantities pL and N have a common factor for any value of p, there is a redundancy in the sampling even for the 1QC. A simulation of a homonuclear system must take into account the highest order of coherence that must be sampled reliably in the calculation. For a system of three or four spin $\frac{1}{2}$ nuclei, a reliable simulation of the effects of a gradient pulse on any achievable order of coherence can be computed using a single loop ($L = 1$) and five segments as a minimum.

Simulations of heteronuclear systems generate interesting complications because of the different gyromagnetic ratios of the nuclei involved. Many heteronuclear experiments employ gradients to cancel and reinforce the phases of two types of nuclei simultaneously; this requires that the arrangement of helix loops and segments used for a simulation sample an integral number of loops in the precession of each nucleus. This can be arranged by (1) adjusting the ratio of the gyromagnetic ratios for the pertinent nuclei to be a rational fraction, and (2) choosing the number of loops also to be in that ratio. Consider an HF spin system which has, to a good approximation, $\gamma_F/\gamma_H = 16/17$. If 17 loops are chosen for the proton phase helix during a particular gradient, then a phase helix for the fluorine nuclei of 16 loops will develop during that same gradient. Care must also be taken in choosing the number of segments. If N were chosen to be 16 in this proton–fluorine example, then the fluorines would be aligned at the same point

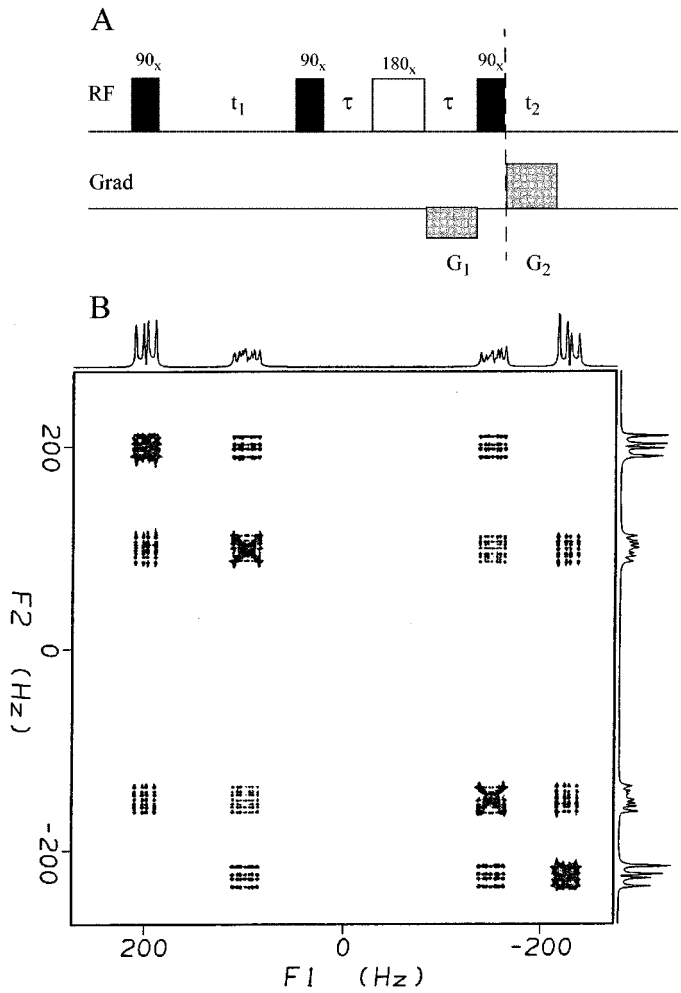

FIG. 3. (A) Pulse sequence for a gradient double quantum filtered COSY experiment from Ref. *31*; (B) simulation of an experiment done with the pulse sequence shown. The RF pulses were assumed to be ideal; the strengths of the first and second gradients were 5 and 10 G/cm, respectively, and of duration 1 ms. The four-spin model system used in the calculation has shifts $\nu_1 = 200.0$ Hz, $\nu_2 = 100.0$ Hz, $\nu_3 = -150.0$ Hz, $\nu_4 = -225$ Hz, and coupling constants $J_{12} = J_{34} = 12.0$ Hz, $J_{13} = J_{24} = 8.0$ Hz, $J_{14} = 0.0$ Hz, and $J_{23} = 5.0$ Hz. The geometry was that of two adjacent methylene groups. Dipole–dipole relaxation assuming a rotational diffusion constant of 5.0×10^8 s^{-1} and random field effects with an interaction constant of 0.1 s^{-1} were included. A single free induction decay was calculated for each t_1 value. A single loop with 18 phase angle segments was used. Acquisition was started immediately after the final 90° pulse (during the final gradient). The plots show positive and negative contours. All cross peaks appeared in absorption as expected. A similar calculation with five slices gave essentially the same results.

in their precessional motion in each loop; in effect, there would be no sampling of phase at all for this nucleus.

The analog of Equation [10] for a heteronuclear system is

$$\theta_k = 2\pi \frac{\{\sum_{a}^{\text{in the coherence}} \gamma_a\}}{\gamma_H}\frac{L_H}{N}k, \quad k = 0, 1, 2, \ldots, N-1, \qquad [11]$$

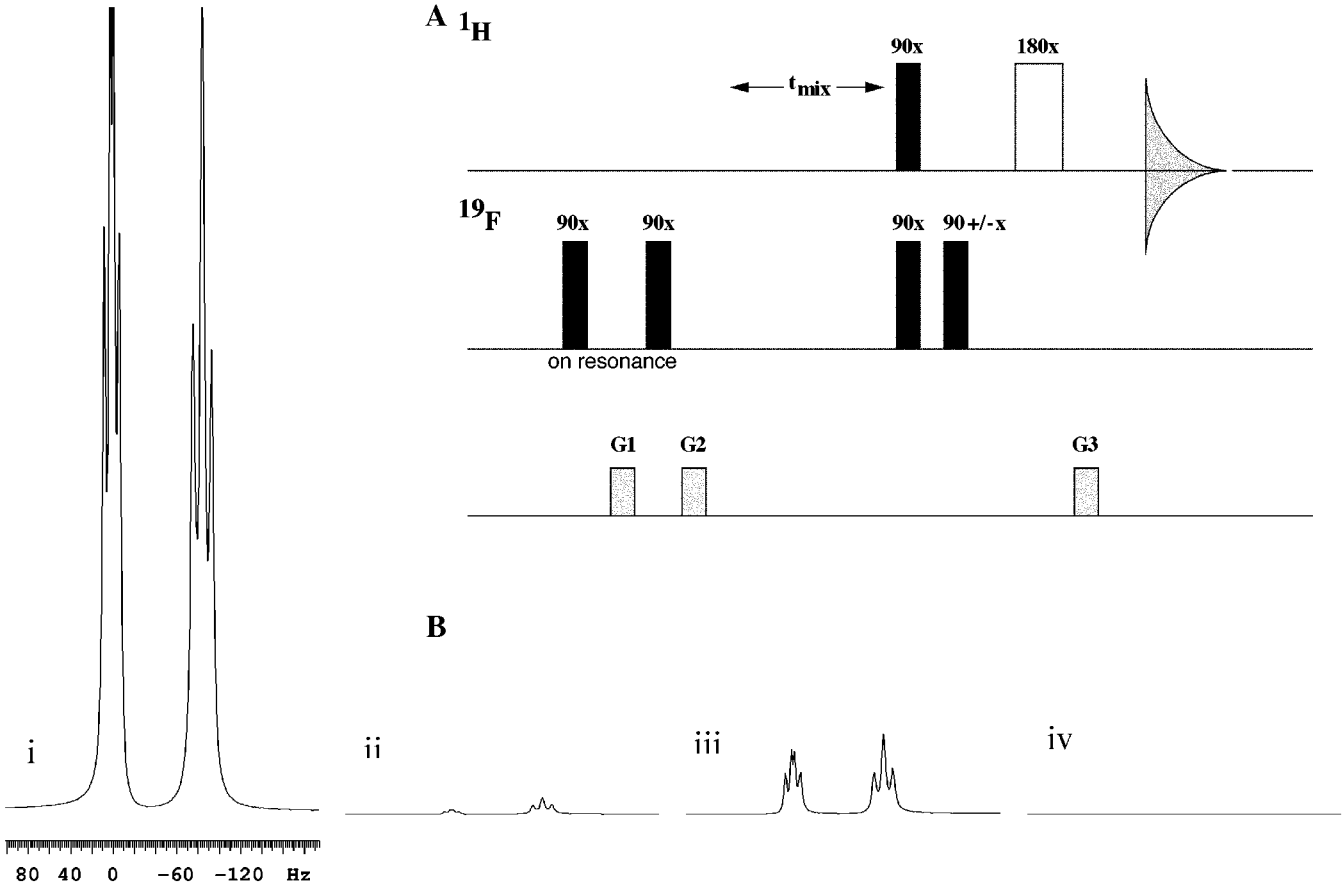

FIG. 4. (A) Pulse sequence for a $^{1}H\{^{19}F\}$ heteronuclear NOE experiment. A 3-spin model corresponding to the fluorine plus the 2- and 3-protons of fluorobenzene was used. Atomic positions were computed from standard bond lengths (*34*). Chemical shifts and coupling constants appropriate to a fluorinated aromatic ring were used. The rotational correlation time was chosen to be 15 ns, a value consistent with a protein of ~30 kDa mass. For each mixing time, two FIDs are calculated and added, corresponding to the 90_x90_x and 90_x90_{-x} phase combinations for the last fluorine 90° pulses. (B) Calculated $^{1}H\{^{19}F\}$ NOE spectra at 500 MHz for the model system described. (i) Calculated proton spectrum of the system obtained with single proton 90° pulse; (ii–iv) spectra of the system with 0.1, 0.8, and 2000 s mixing times. (The proton closest to the fluorine appears upfield.) All plots have the same vertical scale. Computed FIDs were processed without apodization. The 90° pulses used had a duration of 10 μs. The gradients G_1 and G_2 were 10 and 20 G/cm; $G_3/G_1 = \gamma_F/\gamma_H$.

where the sum is over the gyromagnetic ratios of all nuclei involved in a coherence. Here we have used L_H to denote the number of loops for the protons. The number of segments used for the simulation (N) will have to be chosen so it is not a factor of $(\Sigma_a \gamma_a)/\gamma_H$ for any coherence whose response to a gradient must be computed correctly. Notice in particular that a heteronuclear "zero quantum coherence" precesses at a Larmor frequency corresponding to the difference of the Larmor frequencies of the nuclei involved.

As presently carried out, our computations are referenced to the laboratory coordinate system. Thus, a rotation designated $R_x(\theta)$ is a rotation about the lab x-axis. This must be reconciled with the usual convention that a $(\theta)_x$ pulse is a rotation of θ about the x-axis in the frame rotating at the spectrometer frequency for the nuclei of interest. We eliminate this problem in a pragmatic way by arranging that every time interval in the simulation be an integral multiple of the Larmor period of the spectrometer frequency for each type of nucleus. Using this procedure, all rotating frames are coincident with the lab frame at the end of each interval in the simulation. We carry out this arrangement by choosing a small time step (on the order of microseconds) and require that every time interval in the experiment is a multiple of that time step. The gyromagnetic ratio of each nucleus is adjusted (slightly) so that its Larmor period is evenly divisible by the chosen time step. In practice, the proton frequency of the simulation is set to a round number (e.g., 500,000,000 Hz); the required adjustments in the gyromagnetic ratios for other nuclei are less than the experimental uncertainties in those numbers.

In some experiments, certain time intervals are determined by parameters of the spin system such as spin–spin coupling constants. In these cases, we might have to adjust those parameters, so that $J/2\pi$, for example, will be an exact multiple of the chosen time step. Again, the necessary changes are negligibly small.

A Fortran computer program based on the approaches de-

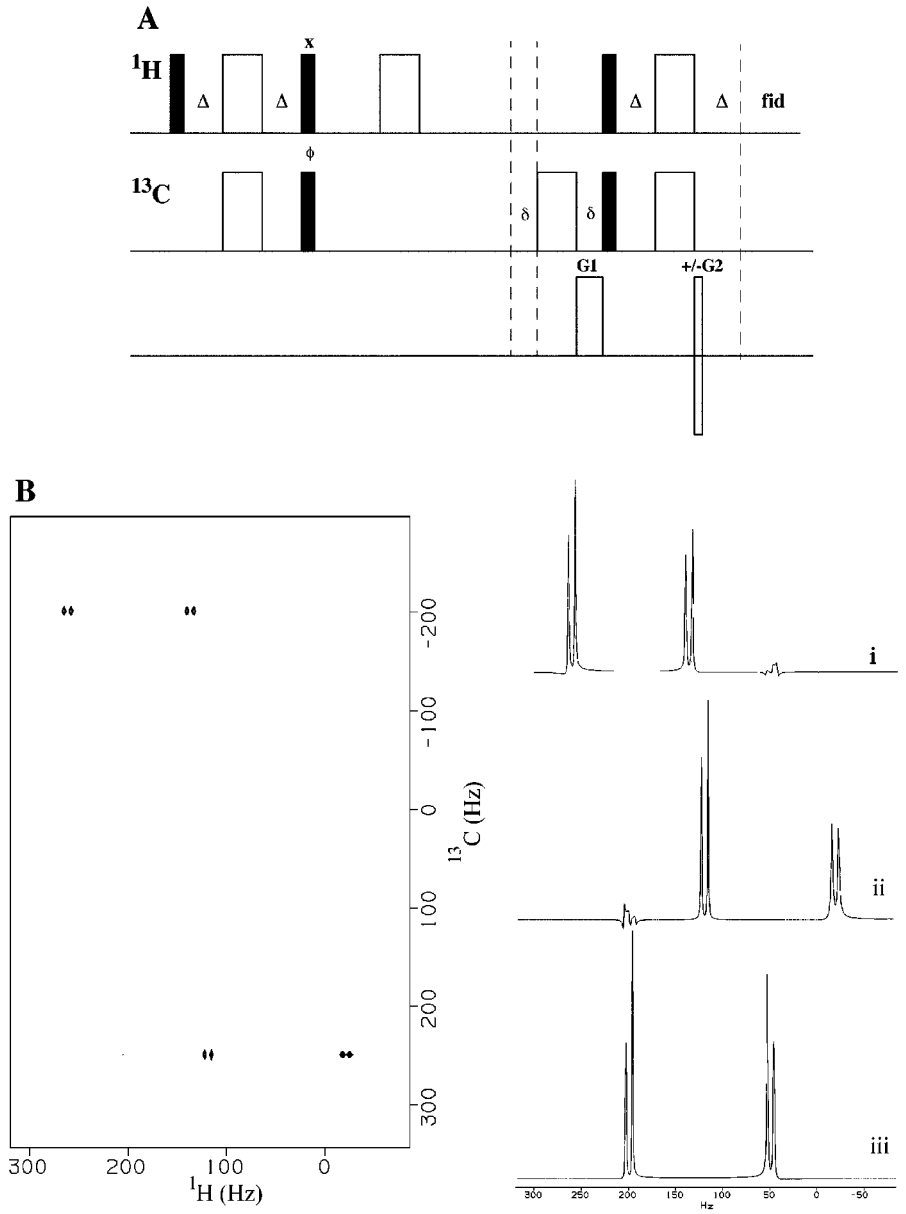

FIG. 5. (A) Pulse sequence for a C–H heteronuclear single quantum coherence experiment (HSQC) with the fragment H_1–C_1–C_2–H_2. Chemical shifts were 50 and 200 Hz for H_1 and H_2, −200 and 250 Hz for C_1 and C_2. $^1J_{C1H1} = 125$ Hz; $^1J_{C2H2} = 140$ Hz; $^2J_{C1H2} = {}^2J_{C2H1} = 5$ Hz; $J_{HH} = 7$ Hz. Two FIDs were accumulated and added for each t_1 step, one for each sign of G_2. $\Delta = 1.89$ ms. In addition to dipole–dipole relaxation, CSA was included on H_1 and C_1: $\delta_{zz}(H) = -118$ ppm, $\eta(H) = -0.0085$, $\delta_{zz}(C) = -116$ ppm, $\eta(C) = -0.431$. Rotational diffusion constants of 2.5×10^9 s^{-1} were assumed. The RF pulses were chosen to be ideal, and TPPI cycling of the first carbon 90° pulse was carried out. The gradients were 10.0 and 2.5 G/cm, respectively, and each had a duration of 1.0 ms. (B) The simulated spectra at 500 MHz. Transsections (i) and (ii) of the 2D map are taken at −200 and 250 Hz, respectively. Trace (iii) is the computed proton spectrum of the ^{12}C isotopomer. Filled rectangles represent 90° pulses while empty rectangles represent 180° pulses on the top two lines.

scribed above was used to simulate some standard one- and two-dimensional high-resolution NMR experiments with gradients. To assess our algorithm, the responses of spin systems to a variety of simple sequences were tested. The output of the test experiment $[(\pi/2)_x$:Grad(τ):fid] was 15 orders of magnitude less than the result of the same simulation when the gradient of length τ was replaced by a simple free precession delay of the same length. For any number of segments ($N > 1$), the spins in segment k will have precessed through $2\pi k/N$ relative to $k = 0$, so the total signal vanishes, to within numerical roundoff error, because

$$\sum_{k=0}^{N-1} \sin 2\pi \frac{k}{N} = \sum_{k=0}^{N-1} \cos 2\pi \frac{k}{N} = 0.$$

Figure 2 shows the results of a simulation of a gradient-recalled

echo sequence applied to a system (*29*) where cross terms between the dipole–dipole and CSA relaxation mechanisms produce significant lineshape effects. These are evident in comparison of spectrum (i) to spectra (ii) and (iii) in Fig. 2. Similar tests were performed to verify that multiple quantum coherences were also refocused correctly.

Pulsed field gradients can be used in COSY-type experiments for coherence selection and thereby provide a means to reduce the experimental time required because phase cycling is not needed. The gradient homonuclear double-quantum filtered COSY experiment proposed by Davis *et al.* (*31*) was simulated (Fig. 3). A product operator description of the experiment leads to the term below for the density matrix in slice k for a two-spin system after the final gradient:

$$\zeta_1^q \zeta_2^{q'} e^{-i[(p+p')G_1+(q+q')G_2]\gamma\tau(k\delta z)}. \qquad [12]$$

Here ζ^q are the raising ($q = +1$), lowering ($q = -1$), and z-component ($q = 0$) spin operators; slices have thickness δz, so ($k\ \delta z$) is the z-coordinate; gradient strengths are G and their duration is τ; p, p', q, and q' are coherence orders. Focusing requires that the phases in various slices reinforce, so $(p + p')G_1 = -(q + q')G_2$ is required for these bilinear terms. Signal is generated only for $q + q' = 1$ during acquisition. In the experiment shown, $|G_2| = 2|G_1|$, so only those terms with $p + p' = \pm 2$ will be converted into single quantum coherence during acquisition. Because either $p + p' = -2$ or $p + p' = +2$ (but not both) can be refocused by the choice of sign for the second gradient, the resulting signal is attenuated by a factor of 2 relative to the signal in a nongradient procedure.

A variety of gradient-enhanced heteronuclear NOE experiments have been proposed: Especially useful ones are of the proton-detected ("inverse") type (*32, 33*), and these are of interest in attempts to detect ^{1}H{^{19}F} NOEs in fluorine-containing biological systems. A scheme for using gradients to this end is shown in Fig. 4. Fluorine coherences are labeled by the first gradient and then converted to z-magnetization. Proton–fluorine cross-relaxation transfers magnetization to the protons. The proton 90° pulse then rotates proton z-magnetization to the transverse plane, where it is refocused by the gradient labeled G3. In order for refocusing of proton coherences to be successful, gradients G1 and G3 must be in the ratio of the proton and fluorine gyromagnetic ratios. A proton 180° pulse is included to refocus proton chemical shift evolution during G3. Because a potential application of this sequence is in biological systems where both dipolar and CSA effects cause rapid relaxation of the fluorine transverse magnetization, refocusing of fluorine coherence is avoided during the first part of the sequence by setting the fluorine carrier frequency on resonance with the fluorine signal. In spin coupled systems, I_zS_z-type magnetization remains at the end of the second fluorine pulse and is not removed by the gradient G2. This will convert to antiphase components in the detected proton signal. Following the design of Stott and Keeler (*33*), additional fluorine pulses are therefore present at the start of the proton detection part of the sequence; alternate FIDs are added in which phases of these pulses are 90_x90_x and 90_x90_{-x}, respectively, to cancel the antiphase components.

As discussed above, simulations of mixed fluorine and hydrogen spin systems require careful consideration in those parts of the calculation intended to represent the effects of gradients. In this example, we sample 17 loops of the phase helix for the hydrogens, which concomitantly samples precisely 16 loops of the fluorine phase helix if the ratio of the gyromagnetic ratios is set to 16/17. For the present experiment, reliable sampling of single quantum coherences of either nucleus is all that is required so that 3, 5, or 7 segments of the proton helix, or any number of segments greater than 9, provide acceptable simulations. However, an error in either the strength or duration of any of the gradient pulses results in noticeably distorted lineshapes.

The simulations shown in Fig. 4 were computed with "real" pulses, meaning that the spins are exposed to a specific B_1 RF field switched on for a defined time, but calculations done with "ideal" pulses (the effect of a pulse being calculated simply as the effect of the appropriate rotation operator) were essentially superimposable on these results. A rotational correlation time of 15 ns was used for the calculations—this is a typical value for a macromolecule of mass ~30 kDa. At a mixing time of 0.1 s, an ^{1}H{^{19}F} NOE of about 2.2% has developed at the proton closest to the fluorine, although spin diffusion effects are already apparent. At 0.8 s, the spin diffusion process is well advanced. At very long mixing times the (transient) NOE should return to zero, and this expectation is borne out in the simulations. Other experimental designs for ^{1}H{^{19}F} heteronuclear NOEs that do not use gradients for coherence selection, but only for purging unwanted magnetization are possible (*35*); we have shown that simulations of these are in accord with results shown in Fig. 4.

A simulation of a ^{1}H{^{13}C} heteronuclear single quantum coherence (HSQC) experiment is shown in Fig. 5. In designing this simulation, again it was essential to recognize that carbon-13 coherences in the presence of a gradient will trace out their characteristic helix in a longer time than will proton coherences at the same field strength. The single quantum coherence selection requires that $\gamma_C G_1 = \pm\gamma_H G_2$. The simulation was carried out for a mixture of H–^{13}C–C–H and H–C–^{13}C–H with geometry and spin–spin coupling parameters that are appropriate for a substituted alkane. CSA was included on one of the CH groups. The FIDs of the three isotopomers were computed separately and added with weights of 98% H–^{12}C–^{12}C–H and 1% of each of the ^{13}C-containing species, so as to imitate the result of an experiment done at the natural abundance of carbon-13. The resulting spectrum displays cross peaks at the expected (^{1}H, ^{13}C) positions; excellent cancellations of resonances from all protons not directly bound to ^{13}C were obtained. In particular, signals from H–^{12}C–^{12}C–H were several orders of magnitude less than those of the ^{13}C species. Differences in cross peak shapes and intensities caused by the

CSA–dipolar cross-relaxation are difficult to observe in the contour map presentation, but the cross-sections included in Fig. 5 show that these effects are present.

CONCLUSIONS

We have outlined an approach for incorporating z-axis pulsed field gradients into simulations of high-resolution NMR spectra. The methods used include conceptualization of the sample as a series of slices or volume elements along the gradient direction and make heavy reliance on propagators to accelerate the calculations. These are extensions of our previous efforts, and the simulation program retains the ability to incorporate rigorous treatments of RF fields and several relaxation mechanisms. Numerous examples have shown that the approach produces simulations rapidly using contemporary workstations.

It is recognized that the representation of the effects of pulsed field gradients in this work is an idealization, and that experiments with real spectrometers and samples will be subject to inhomogeneities in the Zeeman and B_1 fields, gradient nonlinearities, and timing errors. These experimental realities could be included in simulations by straightforward extension of the present software. In the case of gradient inhomogeneity, the gradient field strengths could be made nonlinear in the z-coordinate, and nonidealities in gradient shape could be simulated by computing the effects of several back-to-back (ideal) rectangular gradients chosen in a manner that represents the nonidealities involved.

Diffusion of spins between volume elements has been neglected in this work, but could easily be incorporated (*12*). Diffusion would result in irreversible dephasing within a volume element, leading to a reduction in refocused magnetization in the computed FID. At a cost of additional computing time, the methods used could be extended to include other types of gradients such as triple-axis (x, y, z) gradients and B_1 gradients, by taking into account the shape of a sample.

Although it is continuously evolving, the Fortran code developed in this work is available from the authors. An early version of the code is available from QCPE (Program 660).

APPENDIX A

Propagators

It is well known that the Liouville–von Neumann equation can be solved if the Hamiltonian is independent of time as

$$\sigma(t_0 + t) = e^{-iHt/\hbar}\sigma(t_0)e^{iHt/\hbar} \qquad [13]$$

or, for a specific density matrix element,

$$\sigma_{\alpha\alpha'}(t_0 + t) = \sum_{\beta\beta'} \langle\alpha|e^{-iHt/\hbar}|\beta\rangle\sigma_{\beta\beta'}(t_0)\langle\beta'|e^{iHt/\hbar}|\alpha'\rangle. \qquad [14]$$

In superoperator space, Eq. [14] can be expressed as a single transformation (*26*, *27*) using a propagator P:

$$\sigma_{\alpha\alpha'}(t_0 + t) = \sum_{\beta\beta'} P_{\alpha\alpha'\beta\beta'}(t)\sigma_{\beta\beta'}. \qquad [15]$$

Equation [15] can be evaluated as a simple matrix multiplication by reindexing the density matrix into a vector with $j = (\alpha - 1)2^n + \alpha'$, etc. Equation [15] then becomes

$$\sigma_j(t_0 + t) = \sum_k P_{jk}(t)\sigma_k(t_0). \qquad [16]$$

The effect of successive steps in an experiment can be evaluated by successive multiplications, i.e.,

$$\sigma_2 = [R \cdot Q \cdot P]\sigma_1, \qquad [17]$$

where P, Q, and R are the propagators for three successive intervals in the pulse sequence.

A step including relaxation is not so straightforward, however, because the resulting $\sigma(t_0 + t)$ depends on more than just a propagator $P(t)$ operating on the initial density matrix $\sigma(t_0)$. Instead,

$$\sigma(t_0 + t) = P(t)\sigma(t_0) + \{1 - P(t)\}\sigma^{\infty}, \qquad [18]$$

where σ^{∞} is the equilibrium density matrix. (In the presence of an RF field, it becomes the steady-state (*36–38*) density matrix.) The form of Eq. [18] appears to thwart the simple multiplication of propagators for successive steps. However, Smith *et al.* (*28*) presented a mathematical trick that makes it possible to incorporate the effect of σ^{∞} into a propagator as well. Here we explain our procedure for implementing this step.

We begin by writing the Redfield equation which describes the relaxation of the density matrix in the appropriate interaction representation (designated by $\hat{}$) (*21*, *24*, *28*, *38*):

$$\frac{d}{dt}\hat{\sigma}_{\alpha\alpha'}(t) = \sum_{\beta\beta'} e^{i(\hat{\omega}_{\alpha\alpha'} - \hat{\omega}_{\beta\beta'})t}R_{\alpha\alpha'\beta\beta'}(\hat{\sigma}_{\beta\beta'} - \hat{\sigma}^{\infty}_{\beta\beta'}). \qquad [19]$$

This equation is often solved by invoking the secular approximation and then diagonalizing the Redfield matrix **R**. The secular approximation can be avoided by transforming out of the interaction representation. Eq. [19] then becomes

$$\frac{d\sigma_{\alpha\alpha'}}{dt} = \sum_{\beta\beta'} (R_{\alpha\alpha'\beta\beta'} - i\omega_{\alpha\alpha'}\delta_{\alpha\beta}\delta_{\alpha'\beta'})(\sigma_{\beta\beta'} - \sigma^{\infty}_{\beta\beta'}). \qquad [20]$$

We define a generalized Redfield matrix $\Re$ as

$$\Re_{\alpha\alpha'\beta\beta'} = R_{\alpha\alpha'\beta\beta'} - i\hat{\omega}_{\alpha\alpha'}\delta_{\alpha\beta}\delta_{\alpha'\beta'} \qquad [21]$$

and begin by reindexing Eq. [20] to read

$$\frac{d\sigma_j}{dt} = \sum_k \Re_{jk}(\sigma_k - \sigma_k^\infty). \quad [22]$$

In this form, it is evident that these differential equations can be solved readily if $\Re$ is diagonalized. This can be accomplished by a similarity transformation

$$S^{-1}\Re S = \Lambda = \begin{bmatrix} \lambda_1 & 0 & \cdots & 0 \\ 0 & \lambda_2 & \cdots & 0 \\ \cdots & \cdots & \cdots & \cdot \\ 0 & 0 & \cdots & \lambda_n \end{bmatrix} \quad [23]$$

and Eq. [22] solved in terms of the transformation matrix S and the transformed density matrix ρ; $\rho_l = \Sigma_k S_{lk}^{-1}\sigma_k$. The matrices S and S^{-1} are independent of time, so $S^{-1}d\sigma/dt = d/dtS^{-1}\sigma = d/dt\rho$. In terms of ρ,

$$\frac{d\rho}{dt} = S^{-1}\Re S(\rho - \rho^\infty). \quad [24]$$

Or, in more detail and taking advantage of the diagonalization:

$$\frac{d\rho_l}{dt} = \lambda_l(\rho_l - \rho_l^\infty). \quad [25]$$

This is readily solved to give

$$\rho_l(t) = \rho_l^\infty + e^{\lambda_l t}(\rho_l(0) - \rho_l^\infty). \quad [26]$$

We can regenerate σ from $\sigma = S\rho$, noting that

$$\begin{aligned}\sigma_k(t) &= \sigma_k^\infty + \sum_l S_{kl}e^{\lambda_l t}\sum_j S_{lj}^{-1}(\sigma_j(0) - \sigma_j^\infty) \\ &= \sum_{lj} S_{kl}(1 - e^{\lambda_l t})S_{lj}^{-1}\sigma_j^\infty + \sum_{lj} S_{kl}e^{\lambda_l t}S_{lj}^{-1}\sigma_j(0) \\ &= \sum_{lj} S_{kl}\{(1 - e^{\lambda_l t})S_{lj}^{-1}\sigma_j^\infty + e^{\lambda_l t}S_{lj}^{-1}\sigma_j(0)\}. \quad [27]\end{aligned}$$

Define T_{ln} so that

$$\sum_n T_{ln}\sigma_n(0) = \sum_j (1 - e^{\lambda_l t})S_{lj}^{-1}\sigma_j^\infty \quad [28]$$

and reindex this to give

$$\sum_{\beta\beta'} T_{\alpha\alpha'\beta\beta'}\sigma_{\beta\beta'}(0) = \sum_{\gamma\gamma'} (1 - e^{\lambda_{\alpha\alpha' t}})S_{\alpha\alpha'\gamma\gamma'}^{-1}\sigma_{\gamma\gamma'}^\infty. \quad [29]$$

Taking advantage of the trace of the density matrix $\Sigma_{\beta\beta}\hat{\sigma}_{\beta\beta} = 1$ (this condition can and must be arranged), we need

$$T_{\alpha\alpha'\beta\beta'} = \delta_{\beta\beta'}\sum_{\gamma\gamma'} (1 - e^{\lambda_{\alpha\alpha' t}})S_{\alpha\alpha'\gamma\gamma'}^{-1}\sigma_{\gamma\gamma'}^\infty \quad [30]$$

Then operating on any density matrix with unit trace, T has the desired property:

$$\begin{aligned}\sum_{\beta\beta'} T_{\alpha\alpha'\beta\beta'}\sigma_{\beta\beta'} &= T_{\alpha\alpha' 11}\mathrm{Trace}(\sigma) \\ &= \sum_{\gamma\gamma'} (1 - e^{\lambda_{\alpha\alpha' t}})S_{\alpha\alpha'\gamma\gamma'}^{-1}\sigma_{\gamma\gamma'}^\infty. \quad [31]\end{aligned}$$

Therefore,

$$\sigma_k(t) = \sum_{lj} S_{kl}\{T_{lj} + e^{\lambda_l t}S_{lj}^{-1}\}\sigma_j(0), \quad [32]$$

which enables us to define

$$P_{kj} \equiv \sum_l S_{kl}\{T_{lj} + e^{\lambda_l t}S_{lj}^{-1}\}, \quad [33]$$

so that finally the density matrix can be propagated by operation only on the initial density matrix:

$$\sigma_k(t) = \sum_j P_{kj}\sigma_j(0). \quad [34]$$

In detailed indexing,

$$\begin{aligned}P_{\alpha\alpha'\beta\beta'} = \sum_{\gamma\gamma'} S_{\alpha\alpha'\gamma\gamma'}\{\delta_{\beta\beta'}\sum_{\kappa\kappa'} (1 - e^{\lambda_{\gamma\gamma' t}})S_{\gamma\gamma'\kappa\kappa'}^{-1}\sigma_{\kappa\kappa'}^\infty \\ + e^{\lambda_{\gamma\gamma' t}}S_{\gamma\gamma'\beta\beta'}^{-1}\}, \quad [35]\end{aligned}$$

and it is clear that propagators such as this can be multiplied in tandem to generate a single propagator for a sequence of steps.

APPENDIX B

Calculation of FIDs

In a simulation the calculation of the acquired FID is a repetitive step that can be done efficiently with the propagators discussed in Appendix A. The task at hand is to evaluate the observable magnetization M at equally spaced intervals of time, the "dwell time" t_d,

$$\langle M(nt_d)\rangle = \mathrm{Tr}(M\sigma(nt_d)) = \sum_{\alpha\alpha'} M_{\alpha\alpha'}^{\mathrm{T}}\sigma_{\alpha\alpha'}(nt_d) \quad [36]$$

Although one could step $\sigma(0)$ through the FID collection using

$\sigma(nt_d) = P[\sigma((n-1)t_d)]$, there is a more economical way. Begin with Eq. [27] evaluated at the nth point of the FID

$$\sigma_k(nt_d) = \sigma_k^\infty + \sum_l S_{kl} e^{\lambda_l n t_d} \sum_j S_{lj}^{-1}(\sigma_j(0) - \sigma_j^\infty). \quad [37]$$

Thus,

$$\langle M(nt_d)\rangle = \mathrm{Tr}(M\sigma^\infty) + \sum_k M_k^T \sum_l S_{kl} e^{\lambda_l n t_d} \times \sum_j S_{lj}^{-1}(\sigma_j(0) - \sigma_j^\infty). \quad [38]$$

The last term in Eq. [38] is evaluated by rearranging the summation and defining

$$A_l \equiv \sum_k M_k^T S_{kl} \sum_j S_{lj}^{-1}(\sigma_j(0) - \sigma_j^\infty), \quad [39]$$

which need be computed only once. The magnetization of σ^∞ is likely to be zero, but in any case it, too, needs to be computed only once.

Thus, $\langle M(nt_d)\rangle$ is evaluated with a single "vector" product,

$$\langle M(nt_d)\rangle = \mathrm{Tr}(M\sigma^\infty) + \sum_l e^{\lambda_l n t_d} A_l. \quad [40]$$

The exponential is evaluated for the first dwell step and subsequent steps need only a multiplication $[e^{\lambda_l(n+1)t_d} = e^{\lambda_l n t_d} e^{\lambda_l t_d}]$. Finally, as pointed out in Ref. (*28*), most matrix elements of the operator corresponding to the observable magnetization (typically I_-) vanish. Hence, most of the elements of M are zero, and the evaluation of A is simplified further.

ACKNOWLEDGMENTS

This work was supported in part by the National Institutes of Health, grant GM-44558. Dr. Burton S. Garbow provided very helpful mathematical advice.

REFERENCES

1. E. O. Stejskal and J. E. Tanner, *J. Chem. Phys.* **42,** 288 (1965).
2. A. A. Maudsley, A. Wokaun, and R. R. Ernst, *Chem. Phys. Lett.* **55,** 9 (1978).
3. A. Bax, P. G. De Jong, A. F. Mehlkopf, and J. Schmidt, *Chem. Phys. Lett.* **69,** 567 (1980).
4. L. E. Kay, M. Ikura, and A. Bax, *J. Magn. Reson.* **89,** 496 (1990).
5. J. J. Norwood, *Chem. Soc. Rev.* **23,** 59 (1994).
6. P. Mansfield and B. Chapman, *J. Magn. Reson.* **72,** 211 (1987).
7. R. E. Hurd, *J. Magn. Reson.* **87,** 422 (1990).
8. B. K. John, H. D. Plant, and R. E. Hurd, *J. Magn. Reson. A* **101,** 113 (1993).
9. P. C. M. van Zijl and C. T. W. Moonen, *J. Magn. Reson.* **88,** 28 (1990).
10. P. C. M. van Zijl and C. T. W. Moonen, *NMR Basic Principles and Progress* **26,** 67 (1992).
11. P. J. Hore, *Methods Enzymol.* **176,** 64 (1989).
12. J. Keeler, R. T. Clowes, A. L. Davis, and E. D. Laue, *Methods Enzymol.* **239,** 145 (1994).
13. D. Canet, J. Brondeau, E. Mischeler, and F. Humbert, *J. Magn. Reson. A* **105,** 239 (1993).
14. M. Piotto, V. Saudek, and V. Skelnar, *J. Biomol. NMR* **2,** 661 (1992).
15. K. Scott, J. Stonehouse, J. Keeler, T.-L. Hwang, and A. J. Shaka, *J. Am. Chem. Soc.* **117,** 4199 (1995).
16. A. Bax and S. S. Pochapsky, *J. Magn. Reson.* **99,** 638 (1992).
17. G. W. Vuister, G. M. Clore, A. M. Gronenborn, R. Powers, D. S. Garrett, R. Tschudin, and A. Bax, *J. Magn. Reson. B* **101,** 210 (1993).
18. R. Tolman and J. H. Prestegard, *Concepts in Magn. Reson.* **7,** 247 (1995).
19. L. E. Kay, *Prog. Biophys. Mol. Biol.* **63,** 277 (1995).
20. R. R. Ernst, G. Bodenhausen, and A. Wokaun, "Principles of Magnetic Resonance in One and Two Dimensions," Oxford University Press, Oxford (1987).
21. S. A. Smith, W. E. Palke, and J. T. Gerig, *Concepts in Magn. Reson.* **4,** 107 (1992).
22. S. A. Smith, W. E. Palke, and J. T. Gerig, *Concepts in Magn. Reson.* **4,** 181 (1992).
23. S. A. Smith, W. E. Palke, and J. T. Gerig, *Concepts in Magn. Reson.* **5,** 151 (1993).
24. S. A. Smith, W. E. Palke, and J. T. Gerig, *Concepts in Magn. Reson.* **6,** 137 (1994).
25. A. G. Redfield, *Adv. Magn. Reson.* **1,** 1 (1965).
26. J. Jeneer, *Adv. Magn. Reson.* **10,** 1 (1982).
27. C. Griesinger, C. Gemperle, O. Sorenson, and R. R. Ernst, *Mol. Phys.* **62,** 295 (1987).
28. S. A. Smith, W. E. Palke, and J. T. Gerig, *J. Magn. Reson. A* **106,** 57 (1994).
29. S. G. Withers, N. B. Madsen, and B. D. Sykes, *J. Magn. Reson.* **61,** 545 (1985).
30. T. M. Duncan, "A Compilation of Chemical Shift Anisotropies," Farragut, Chicago (1990).
31. A. L. Davis, J. Keeler, E. D. Laue, and D. Moskau, *J. Magn. Reson.* **98,** 209 (1992).
32. W. Bauer, *Magn. Reson. Chem.* **34,** 532 (1996).
33. K. Stott and J. Keeler, *Magn. Reson. Chem.* **34,** 554 (1996).
34. A. J. Gordon and R. A. Ford, "The Chemist's Companion," Wiley, New York (1972), p. 107.
35. J. T. Gerig, submitted.
36. R. A. Hoffman, *Adv. Magn. Reson.* **4,** 87 (1970).
37. B. D. N. Rao, *Adv. Magn. Reson.* **4,** 271 (1970).
38. M. Ravikumar, R. Shukla, and A. A. Bothner-By, *J. Chem. Phys.* **95,** 3092 (1991).